Beiträge zur Tabakforschung International/*Contributions to Tobacco Research* Volume 23 · No. 1 · April 2008
DOI: 10.2478/cttr-2013-0847

Mathematical Modeling of a Lit-End Cigarette: Puffing Cycle and Effects of Puff Counts*

by

M.S. Saidi[1], A. Mhaisekar[2], M.R. Hajaligol[2], and M. Subbiah[2]

[1] *Saidi Partnership, Richmond, Virginia, USA*
[2] *Philip Morris USA Research Center, Richmond, Virginia, USA*

SUMMARY

The burning cycles of a lit-end cigarette were numerically simulated using a 3-D model that includes both the cigarette and its surrounding ambient air and the effects of buoyancy forces. The solid and gas phases were treated separately in a thermally non-equilibrium environment. The tobacco pyrolysis and char oxidation were modeled using multi-precursor models. The changes in tobacco column porosity and its subsequent effects on permeability and gas diffusivity were included. The mass, momentum, energy, and species transport equations were solved in a discretized computational domain using a commercially available computational fluid dynamics (CFD) code. The model was applied to puff a cigarette under different puffing intensities and the effects of puff volume, puff profile, and puff duration were studied. The results show that the model is capable of reproducing the major features of a burning cigarette during both smoldering and puffing. For the puffing and puff-by-puff cases, the solid and gas temperatures as well as those mainstream smoke constituents predicted by the model are in a good agreement with experimental results. A parametric study shows the significant effect of puff volume, puff profile, ventilation rate, and puff counts on solid and gas phase temperatures as well as gaseous species concentrations and mainstream smoke delivery. The buoyancy forces have shown to be very important in both smoldering and puffing. [Beitr. Tabakforsch. Int. 23 (2008) 46–62]

ZUSAMMENFASSUNG

Die Brennzyklen einer glimmenden Zigarette wurden anhand eines 3D-Modells numerisch simuliert, wobei sowohl die Zigarette als auch die Umgebungsluft sowie die Auswirkungen des Luftauftriebs berücksichtigt wurden. Die Partikel- und Gasphasen wurden getrennt in der Umgebung eines thermischen Ungleichgewichts behandelt. Die Tabakpyrolyse und die Kohleoxidation wurden mit einem Multiprecursor-Modell modelliert. Die Veränderungen in der Porosität des Tabaksstrangs und die daraus resultierenden Auswirkungen auf die Permeabilität und die Gasdiffusion wurden hierbei berücksichtigt. Die Masse, der Impuls, die Energie und die Transportgleichungen wurden in einer diskreten rechnerischen Umgebung mit einem handelsüblichen computergestützten CFD-Code berechnet. Mithilfe des Modells wurden die Auswirkungen unterschiedlicher Abrauchintensität einer Zigarette untersucht und die Effekte des Zugvolumens, des Zugprofils und der Zugdauer ermittelt. Die Ergebnisse zeigen, dass die wichtigsten Eigenschaften einer brennenden Zigarette während eines Zuges und der Zugpausen mithilfe des Modells reproduziert werden können. In beiden Fällen befanden sich sowohl die Temperaturen in der Gas- und der Partikelphase als auch die Komponenten des Hauptstromrauchs, die durch das Modell vorhergesagt wurden, in guter Übereinstimmung zu den experimerimentellen Ergebnissen. Eine parametrische Untersuchung zeigt signifikante Auswirkungen des Zugvolumens, des Zugprofils, der Ventilation und der Zugzahl auf die Temperatur der Gas- und Partikelphase als auch auf die Konzentrationen einzelner Verbindungen in der Gasphase und auf die Hauptstromrauchausbeute. Die Impulskräfte erwiesen sich sowohl in den Zugpausen als auch während eines Zuges als sehr bedeutsam. [Beitr. Tabakforsch. Int. 23 (2008) 46–62]

RESUME

Les cycles de combustion d'une cigarette allumée ont été simulés numériquement par un modèle en 3D, comprenant la cigarette avec l'air ambiant et les effets de poussée. Les

*Received: 20th December 2006 – accepted: 18th January 2007

phases solide et gazeuse sont examinées séparément dans un environnement thermique non équilibré. La pyrolyse du tabac et l'oxydation du carbone ont été modélisées par des modèles multi-précurseurs. Les changements de la porosité du boudin de tabac et son effet sur la perméabilité et la diffusion gazeuse sont inclus. La masse, le moment, l'énergie et des équations de transport des molécules ont été calculées par un modèle numérique discret à l'aide de la technique informatique CFD. Le modèle a été appliqué pour fumer une cigarette sous des intensités et volumes de bouffée différents, le profil de bouffée et la durée de bouffée ont été étudiés. Les résultats révèlent que le modèle permet de reproduire les caractéristiques principales d'une cigarette lors de la combustion libre et pendant les bouffées. Dans les deux cas, les températures des phases solide et gazeuse et les composants de la fumée principale prédits par le modèle sont en bon accord avec les résultats expérimentaux. Une étude paramétrique révèle l'effet significatif du volume de bouffée, du profil de la bouffée, du taux de ventilation et du nombre des bouffées sur les températures des phases solide et gazeuse, sur les teneurs en composants gazeuses et en composants dans la fumée principale. Les effets de poussée se sont révélés très importants lors de la combustion libre et pendant les bouffées. [Beitr. Tabakforsch. Int. 23 (2008) 46–62].

INTRODUCTION

Modeling smoldering and puffing of a cigarette has a history of several decades of effort and dates back to as early as the 1960's by EGERTON *et al.* (1). They studied the physical mechanism of cigarette smoldering to elucidate the dependence of temperatures, consumption rates, etc., on cigarette structure and smoldering parameters. Since then there have been numerous efforts in this area worldwide as discussed below. Modeling of a burning cigarette can be classified into two approaches, empirical and theoretical. In the empirical approaches, the available experimental data are generally fitted to a mathematical correlation. The theoretical approach attempts to construct a model that is based on first principles, i.e., mass, momentum and energy balances. In this work, we primarily discuss the theoretical approach.

The different processes and mechanisms involved in smoldering in general and specifically in the burning of a cigarette were reviewed in detail by OHLEMILLER (2). Until recently, mathematical modeling pertaining to a smoldering and puffing cigarette was primarily done with one and two-dimensional geometries. Notable one-dimensional studies in this area are work done by SUMMERFIELD *et al*. (3) on modeling steady-draw smoking, NORBURY and STUART (4) on presenting a transport model for porous medium combustion, KANSA (5) for modeling charring pyrolysis, including porous and permeable structures, Leach *et al*. (6) for presenting a transient model for forward smoldering, MURAMATSU *et al*. (7) for modeling natural smoldering of a cigarette, and SANDUSKY *et al*. (8) for modeling the forced smoldering (puffing) of a cigarette. Among two-dimensional models, one may refer to the work done by DI BLASI (9) for modeling the combustion processes of charring and non-charring solid fuels of slab geometry and Yi *et al*. (10) for developing a steady state model for smoldering of a cylindrical geometry. ROSTAMI *et al*. presented a transient model based on first principles for both natural (11) and forward smoldering (12) of a cigarette which considers the smoldering domain to have two independent phases of solid and surrounding gas interacting at the interfaces. Finally, SAIDI *et al.* presented an experimental and numerical analysis of puff hydrodynamics (13) and also developed a 3-D model to numerically simulate a burning cigarette during puffing (14) based on available temperature distributions inside the cigarette coal.

In the present work we numerically simulate the puffing and smoldering of a cigarette based on first principles in a three-dimensional domain. Even though the cigarette is geometrically symmetric, due to the considerable effect of buoyancy forces, the problem is inherently three-dimensional. This study goes beyond the previous works; it studies the effect of varying physical parameters of puffing such as puff profiles, puff durations, puffing standards and puff-by-puff smoking. In this work, the surrounding air is included in the computational domain, and thus the cigarette-surrounding environment boundary is naturally treated without imposing boundary conditions at the cigarette surface. The boundary condition is imposed on the far field boundary, where the effect of the cigarette is negligible and pressure and temperature can be set to the relevant background values as the boundary conditions.

MATHEMATICAL MODELING

The mathematical modeling is based first principles and solving the partial differential equations of conservations of mass, momentum, and energy for a system containing a conventional cigarette and its surrounding air. The cigarette column is modeled as a porous media. The conservation equations on a macroscopic scale are derived by application of a volume averaging technique to the fundamental microscopic transport equations in a porous media. The air-cigarette boundary is a part of the solution to be determined; an ambient boundary condition is applied on the far field boundary where the effect of the presence of cigarette is negligible, and thus, imposes no pre-conditioning on the final solution.

In this model we have not considered the thermal swelling and/or shrinkage as the solid fuel undergoes pyrolysis and also have neglected volatile species condensation. All gases are assumed to behave according to the ideal gas law.

Tobacco pyrolysis model

Pyrolysis studies (15) have shown that the decomposition products are produced at a rate which is determined entirely by the chemical kinetics; the rate of mass transfer between the reactant surface and the gas phase is very rapid compared with the rate of the chemical decomposition of the tobacco constituents.

Assuming an Arhenius type equation for the pyrolysis of tobacco shreds, the rate of pyrolysis is calculated using 42-precursor kinetic parameters for tobacco provided by WOJTOWICZ *et al*. (16). For a single species *i*, the reaction rate equation is written as (17):

Table 1. Kinetic parameters for tobacco pyrolysis and oxidation and water evaporation used in the simulation (16, 37)

Precursor	A_i (min^{-1})	E_{0i}/R (K)	V_{ci} (wt %)
Kinetic parameters for tobacco char oxidation (19)			
1	2.8×10^6	9813	50
2	1.15×10^{11}	19123	50
Precursor	A_i (s^{-1})	E_{0i}/R (K)	Y_i (wt %)
Kinetic parameters for tobacco moisture evaporation (37)			
1	1.0×10^{12}	9813	100

$$\frac{dV_i}{dt} = K_i(V_{i*} - V_i); \quad K_i = \int_{-\infty}^{+\infty} A_i \exp(-E/RT_s) \frac{\exp(-\frac{1}{2}(E-E_{0i})^2)}{\sigma_i\sqrt{2\pi}} dE \quad [1]$$

After some mathematical manipulation, Eqn. [1] reduces to:

$$K_i = A_i \exp\left[-\frac{E_{0i}}{RT_s}\left(1-\frac{\alpha_i}{T_s}\right)\right]; \quad \alpha_i = \frac{(\sigma_i/R)^2}{2(E_{0i}/R)} \quad [2]$$

$$V_i^{n+1} = V_i^*(1-(1-V_i^n/V_i^*)\exp(-K_i\Delta t)); \quad \Delta t_{n+1} - t_n \quad [3]$$

To gain a second order accuracy in the above calculations K_i is calculated based on new and old values of solid temperature. The volumetric rate of production of each component is calculated as:

$$\Delta\frac{\rho_{py}}{\Delta t} = \rho_{daf}\sum_j \frac{(V_j^{n+1} - V_j^n)}{(t_{n+1} - t_n)} \quad [4]$$

Tobacco char oxidation model

The rate of char production due to pyrolysis is calculated in terms of the total rate of tobacco pyrolysis:

$$\Delta\frac{\rho_{cp}}{\Delta t} = a_c\Delta\frac{\rho_{py}}{\Delta t} \quad [5]$$

where $a_c = 0.17$ for bright tobacco.
We consider the following reaction for char oxidation:

$$C + n_{O_2}O_2 \mapsto n_1 CO + n_2 CO_2 \quad [6]$$

The split between CO and CO_2 a function of temperature and is derived as:

$$R_{CO/CO_2} = \frac{\text{kg mole CO}}{\text{kg mole CO}_2} = \frac{n_1}{n_2} = A_{cc}\exp(-E_{cc}/RT) \quad [7]$$

where $A_{cc} = 200$ and $E_{cc} = 37700$ J/mol · K (18); n_1, n_2, and n_{O_2} were derived in terms of R_{CO/CO_2} as follow:

$$n_1 = \frac{R_{CO/CO_2}}{1+R_{CO/CO_2}}, n_2 = \frac{1}{1+R_{CO/CO_2}}, n_{O_2} = (2+R)/(2+2R) \quad [8]$$

If char oxidation is only kinetically controlled, the MURAMATSU's two equation model (19) is applied to calculate the rate of tobacco char oxidation:

$$\Delta\frac{\rho_{char,k}}{\Delta t} = \rho_{char}^n\sqrt{Y_{O_2}^n}\sum_{i=1}^{2} V_{ci}(-A_i \exp(-E_{i0}/RT_s)) \quad [9]$$

The parameters A_i, E_i and V_{ci}^* are given in Table 1. On the other hand, if char oxidation is only mass transfer controlled, then the rate of char oxidation is controlled by the rate of oxygen transferred to the char. The oxygen concentration on the char surface can be assumed zero and thus:

$$\frac{\Delta\rho_{char,m}}{\Delta t} = n_{O_2} * Y_{O_2}^n * \rho_g^n * A_v * h_m^n / n_{mass} \quad [10]$$

The superscript n refers to time step t_n, n_{O2} was defined in Equation [8], and n_{mass} is a correction factor to include the effects of shred pore diffusion on the overall oxygen mass transfer coefficient. By matching the results of numerical simulation with experiment, this factor can be estimated. For the current simulation, it was found that a value of 2 leads to a good agreement between experimental and modeling results, so it was fixed at 2. The overall rate of char oxidation is determined by the combination of the two above mentioned rates:

$$\frac{\Delta\rho_{char}}{\Delta t} = \left[\left(\frac{\Delta\rho_{char,k}}{\Delta t}\right)^{-1} + \left(\frac{\Delta\rho_{char,m}}{\Delta t}\right)^{-1}\right]^{-1} \quad [11]$$

The net rate of char production is the sum of char produced during pyrolysis and the rate at which it is consumed during char oxidation:

$$\frac{\Delta\rho_c}{\Delta t} = \frac{\Delta\rho_{cp}}{\Delta t} - \frac{\Delta\rho_{char}}{\Delta t} \quad [12]$$

Continuity equation

$$\frac{\partial(\varepsilon\rho_g)}{\partial t} + \vec{\nabla}\cdot(\rho_g\vec{V}) = \text{SOURCE}_{mass} \quad [13]$$

where SOURCE_{mass} is equal to the net mass produced per unit volume per unit time due to moisture evaporation, tobacco pyrolysis and char oxidation.

$$\text{SOURCE}_{mass} = \frac{d\rho_{vm}}{dt} + \frac{d\rho_{we}}{dt} + \frac{d\rho_{CO_2}}{dt} + \frac{d\rho_{CO}}{dt} + \frac{d\rho_{O_2}}{dt} \quad [14]$$

Momentum equation

The general form of momentum equations for incompressible flow in a porous media is given as (19):

$$\frac{\partial(\rho_g \vec{V})}{\partial t} + (\vec{V}\cdot\vec{\nabla})(\rho_g \vec{V}) = -\vec{\nabla}P + \vec{\nabla}\cdot(\mu\vec{\nabla})\vec{V} + \rho_g \vec{g} - \mathrm{SOURCE}_{\mathrm{momentum}} \quad [15]$$

where V is the superficial velocity, the average local velocity, if there is no solid phase.
The source term $\mathrm{SOURCE}_{\mathrm{momentum}}$ represents the added pressure drop due to the presence of solid phase and is given based on the modified ERGUN equation (20):

$$\mathrm{SOURCE}_{\mathrm{momentum}} = \frac{\mu}{K}\vec{V} + \frac{F\rho_g}{K^{1/2}}|\vec{V}|\vec{V} \quad [16]$$

In the above equation, the effect of inertia becomes important for Re > 3. For a packed bed of mono-sized spherical particles the permeability, K, is predicted by Carman-Kozeny model (21):

$$K = \frac{\phi^3 D_p^2}{C_K(1-\phi)^2} \quad [17]$$

where C_K is equal to 1300 for a shredded bed.
The effect of temperature on gas viscosity (μ) is implemented with Sutherland's law (22):

$$\mu = \frac{C_1 T^{3/2}}{T + C_2} \quad [18]$$

where $C_1 = 1.458 \times 10^{-6}$ kg/m·s·$K^{1/2}$ and $C_2 = 110.4$ K.

Energy equation

During the process of puffing, the time variation of the solid temperature is so fast that the assumption of gas-solid thermal equilibrium is no longer valid. Therefore, the two-medium treatment is applied for the energy equation. The solid phase is treated as a continuum, and particle-scale gradients are excluded. The solid- and gas-phase energy equations (23) are:

$$\frac{\partial((1-\phi)\rho_s c_{ps} T_s)}{\partial t} = \vec{\nabla}\cdot\left[(k_{seff} + k_r)\vec{\nabla}T_s\right] + hA_v(T_g - T_s) + \mathrm{SOURCE}_s \quad [19]$$

$$\frac{\partial(\phi\rho_g C_{pg} T_g)}{\partial t} + \vec{\nabla}\cdot(\rho_g \vec{V} C_{pg} T_g) = \vec{\nabla}\cdot\left[(k_{geff} + \phi\rho_g C_{pg} D_t^d)\vec{\nabla}T_g\right] + hA_v(T_s - T_g) \quad [20]$$

where C_{pg} is the mass weighted average specific heat capacity of the gaseous species and the source term SOURCE_s represents the sum of heat of char oxidation, pyrolysis, evaporation, radiation cooling and heat generated by the electric lighter:

$$\mathrm{SOURCE}_S = H_{\mathrm{combustion}}\frac{d\rho^c}{dt} + H_{\mathrm{pyrolysis}}\frac{d\rho_{py}}{dt} + H_{\mathrm{evaporation}}\frac{d\rho_{we}}{dt} + H_{\mathrm{lighter}} + \sigma\varepsilon A_{vr} f_{rad}(T_\infty^4 - T_s^4) \quad [21]$$

The radiation heat exchange with the environment takes place on the coal surface and f_{rad} is set to zero everywhere except in this region where it is set to one. The parameter A_{vr} is the computational cell surface to cell volume ratio and is equal to the cell surface area facing towards the environment divided by the cell volume.
The effective thermal conductivities of the solid and the gas media are calculated based on volumetric average method (24):

$$k_{seff} = (1 - \Phi)\, k_s \quad [22]$$

$$k_{geff} = \Phi\, k_g \quad [23]$$

The simultaneous existence of temperature and velocity gradients within the pore causes spreading of heat, which is separate from Darcian convection and the effective (collective) molecular conduction. Due to volume averaging over the pore space, this contribution is not included in the Darcian convection, and because of its dependence on, it is added as a dispersion coefficient to the effective thermal conductivity (25).
Different models are proposed for determining dispersion coefficient, i.e. (26–29). Here we apply the correlation proposed by VORTMEYER (27) which is close to the ones given by KOCH and BRADY (28) EDWARDS and RICHARDSON (29).

$$D_t^d = 0.8\,\alpha_t\,\mathrm{Re}\,\mathrm{Pr} \quad [24]$$

The mass dispersion coefficient, D_t^d, is calculated from an equation similar to the above equation:

$$D_m^d = 0.8\,\alpha_m\,\mathrm{Re}\,\mathrm{Sc} \quad [25]$$

where α_m is the mass diffusivity of gas species in a media that contains not only other gases but non-fluidic porous medium such as packed tobacco rod, porous wrapper paper, or filter.
The Nusselt number of a packed bed of spherical particles is given by WAKAO correlation (30):

$$\mathrm{Nu}_d = 2 + 1.1\,\mathrm{Re}_d^{0.6}\,\mathrm{Pr}^{0.33} \quad [26]$$

In the above equation the stagnant flow limiting value is sensitive to particle geometry and is 2 for a bed of spherical particles while the flow dependent part is less sensitive (31). Therefore we assume that a bed of shredded bed follows the following correlation:

$$\mathrm{Nu}_d = \mathrm{Nu}_{0b} + 1.1\,\mathrm{Re}_d^{0.6}\,\mathrm{Pr}^{0.33} \quad [27]$$

The bed is made of shreds and each shred has plate type geometry. The stagnant flow Nusselt number for a typical shred is determined using correlation given by (32). On the other hand, the Nusselt number of a s ingle shred and a packed bed of shreds of porosity Φ are correlated as (31):

$$\mathrm{Nu}_{0b} = (1 + 1.5(1-\phi))\,\mathrm{Nu}_0 = 0.7 \quad [28]$$

Based on Reynolds analogy and since in the cases of our interest the Lewis number is close to one, similar correlations are valid for mass transfer coefficient:

Table 2. Thermo-physical and geometrical properties of the cigarette used in the simulation (36, 42–45)

Tobacco column physical properties				
Surface to volume ratio of tobacco (m^{-1})	Surface to volume ratio of ash (m^{-1})	Tobacco particle dimension (m)	Tobacco column porosity	Tobacco column density (kg/m^3)
4400	2000	2.75×10^{-4}	0.8	218
Permeability (m^2)				
Unburned biomass column	Burned biomass column	Unburned Wrapper paper	Burned wrapper paper	Filter
5.6×10^{-10}	1×10^{5}	4.87×10^{-15}	1×10^{5}	2.5×10^{-10}
Some thermo-physical properties				
α_m(air) (m^2/s)	α_m (paper) (m^2/s)	α_m (filter) (m^2/s)	C_{ps} (KJ/kg × K)	k_s (W/m × K)
2.1×10^{-5}	4.68×10^{-7}	2.7×10^{-7}	1.38	0.27
Tobacco shred density (kg/m^3)				
ρ_s	ρ_{daf}	ρ_{we}	ρ_{char}	ρ_{ash}
1090	931.5	109	177	49.7
Heat rates				
$H_{combustion}$ (J/kg)	$-H_{pyrolysis}$ (J/kg)	$-H_{evaporation}$ (J/kg)	$H_{lighter}$ (W)	
1.76×10^{7}	2.09×10^{5}	2.26×10^{6}	2.0×10^{8}	

$$\mathrm{Sh_d} = \mathrm{Sh_{0b}} + 1.1\,\mathrm{Re_d^{0.6}\,Sc^{0.33}}; \qquad \mathrm{Sh_{0b}} = 0.7 \qquad [29]$$

In the cigarette coal where the solid temperature is as high as 1200 K, the radiation heat transfer mechanism should be considered. Assuming the gas participation in radiation heat transfer to be negligible, the solid-solid radiative heat transfer is compensated by adding an equivalent term, K_r to the solid phase effective thermal conductivity in the solid energy equation (33):

$$k_r = 4FD_p\sigma T_s^3;$$

$$F = 0.1843 + 0.5756\tan^{-1}\left[\frac{1.535}{\varepsilon_r}\left(\frac{k_s}{4D_p\sigma T_s^3}\right)^{0.8011}\right] \qquad [30]$$

Gaseous species transport equations

Having the velocity flow field, the gaseous species concentrations are determined by solving the gas transport equation in a porous media for each species (34):

$$\frac{\partial(\rho_g\phi Y_i)}{\partial t} + (\vec{V}\cdot\vec{\nabla})(\rho_g Y_i) = \vec{\nabla}\cdot\left[\rho_g\phi\,(D_{gi} + D_m^d)\vec{\nabla}Y_i\right] + \mathrm{SOURCE_i} \qquad [31]$$

The source term $SOURCE_i$ is the sum of the volumetric rate of production/consumption of gaseous species *i* due to evaporation, pyrolysis and char oxidation.

The gas diffusivity is a function of gas temperature and pressure. For a gas mixture the Fuller-Schettler-Giddings binary mixture model (35) is used for determining the mass diffusion coefficients. In the porous media the mass diffusivity decreases with bed porosity and its effect is considered as (36):

$$D_{AB} = d_{AB}\,\phi^{1.18} \qquad [32]$$

Moisture evaporation

The moisture evaporation is represented as a heterogeneous reaction between liquid water and vapor (37):

$$\frac{d\rho_{we}}{dt} = -K_{we}\rho_{we}; \qquad K_{we} = A_{we}\,\exp\,(-E_{we}/\mathrm{RT}) \qquad [33]$$

where $A = 5.13 \times 10^6\ s^{-1}$ and $E = 24$ KJ/mol for wood particles free water. We apply the same parameters for tobacco shred and neglect the effect of bound water.

Physical properties

The physical properties of the tobacco column are depicted in Table 2. The solid-gas interfacial area per unit volume based on equivalent spherical particle diameter is given as:

$$A_V = 6(1 - \Phi)/D_P \qquad [34]$$

As the cigarette burns, its permeability, porosity, and solid-gas interfacial area change. Also during the burning process the tobacco column packing density change. This change is determined by calculating the mass lost due to moisture evaporation, pyrolysis, and char oxidation.

$$\frac{d\rho_b}{dt} = -\frac{\Delta\rho_{py}}{\Delta t} - \frac{\Delta\rho_{char}}{\Delta t} - \frac{\Delta\rho_{we}}{\Delta t} \qquad [35]$$

The change in bed permeability, porosity, and solid-gas interfacial area is derived by assuming a linear correlation between bed density change and the above mentioned changes:

$$\phi = \phi_{ash} + (\phi_0 - \phi_{ash})\left(\frac{\rho_b - \rho_{ash}}{\rho_{0b} - \rho_{ash}}\right) \qquad [36]$$

$$K = K_{ash} + (K_0 - K_{ash})\left(\frac{\rho_b - \rho_{ash}}{\rho_{0b} - \rho_{ash}}\right) \qquad [37]$$

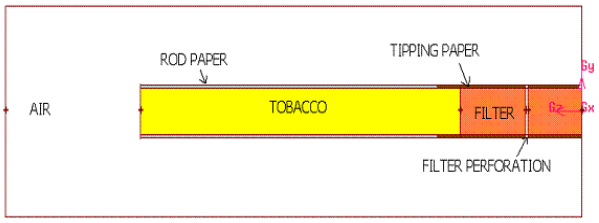

Figure 1. Schematic of the computational domain

$$A_v = A_{ash} + (A_0 - A_{ash}) \left(\frac{\rho_b - \rho_{ash}}{\rho_{0b} - \rho_{ash}} \right) \quad [38]$$

The subscript 0 refers to the initial values of the packed bed.

The ash formation

Once the char is completely burned, ash is remained. Mathematically ash is set equal to current value of solid density once the char density has decreased to less than 5% of its maximum value. The ash is considered to be inert with no participation in the energy equation, presenting negligible resistance to flow and high porosity.

Numerical method

The transport equations were numerically solved using the commercially available computational fluid dynamic code, Fluent 6.0.2. Fluent uses a control-volume-based technique. The pressure and velocity coupling are done through the continuity equation by use of the Simplec (38) algorithm. The second order scheme, Quick (39), was chosen for momentum flux calculation through an implicit segregated solver. In order to handle the multi-phase media; Fluent was customized by utilizing its User Defined Function (40). This was necessary to separately calculate the changes in both the gas- and solid-phase temperatures.

RESULTS AND DISCUSSIONS

The puffing and smoldering cycle of a cigarette is analyzed and the results are presented in this current section. A cigarette is numerically smoked with a 2 s sinusoidal puff followed by 3 s of smoldering and the results of the second puff are presented, comprising one puffing and smoldering cycle for the base case. Variation in puff parameters is presented next, having three different puff profiles, changing the duration of puff and employing three different puffing intensities. Finally the puff-by-puff simulation is performed representing results for various puff number, i.e. 2nd, 4th, 6th and 8th puff.

Due to the presence and effectiveness of buoyancy forces, the flow dynamics of smoldering and puffing a cigarette is a three-dimensional problem, except for the special case where the cigarette axis is aligned with gravity. However, the problem is symmetric with respect to a vertical plane passing through the cigarette axis. Therefore the computational domain in the present analysis comprises only the half of the physical domain. Figure 1 shows the computational domain along the plane of symmetry. In order to make the computational domain grid independent, a grid study was performed and the proper domain and grid size were chosen that optimized speed without compromising on the accuracy.

Basic features of a burning cigarette during puffing and smoldering

In this section, the results of simulating the second puff of a cigarette followed by smoldering are presented. The puff profile is sinusoidal with 2 s duration and a puff volume of 35 cc. During the lighting of a cigarette, heat is delivered to the tobacco column by the lighter. Heat is also generated during char oxidation and is propagated downstream mainly by the hot gases. An increase in temperature in the tobacco column causes an increase in the wrapper paper temperature. In our current model, the wrapper paper is treated as a porous media allowing gases to diffuse into and out of the tobacco column. However, the combustion of paper itself is not modeled. Rather a temperature boundary condition is imposed on the paper such that if the temperature exceeds 773 K (400˚C), the paper is burnt completely and is converted into ash.

In order to compare the behavior of a cigarette during puffing and smoldering, the data corresponding to the peak of the puff (one second after the start of the puff) and three seconds after the end of the puff (smoldering) are chosen. Figure 2a shows the contours of gas temperature on the vertical plane at 1 s into puffing and Figure 2b shows the contours after 3 s of smoldering. Both the figures are plotted on the same scale and the figure is color coded for varying temperature. It can be observed that higher temperatures are noted during puffing (1063 K) as compared to smoldering (822 K). The non-similarity of contours between the upper and lower half of the cigarette, about the axis, show the effect of buoyancy. The coal is hotter along the periphery of the cigarette due to influx of oxygen during puffing. During smoldering the natural convection is the driving force for airflow and brings in fresh oxygen to the coal. The mass flow rate in the coal region during smoldering is much lower compared to puffing and that is the reason lower temperatures are observed.

Figures 3a and 3b show the contours of solid temperature on the vertical plane passing through the center of the cigarette at 1 s after the start of puffing and 3 s after the end of puffing (during smoldering), respectively. It can be observed from the figure that the contours are not symmetric about the axis of the cigarette. The highest temperature of about 1200 K occurs at the lower end of the cigarette below the axis. The circular contours in the region above and below the axis indicate that presence of a hot, donut like shaped region along the periphery of the cigarette. This is due to the fresh air bringing in oxygen along the periphery of the paper burn-line in the cigarette during puffing. The rest of the coal is at a relatively lower temperature. Figure 3b shows the solid temperature contours along the center plane at 3 s after the end of puffing. A difference of about 280 degrees is seen between the maximum temperature during the peak of the puff and smoldering. Also the highest temperature occurs in the

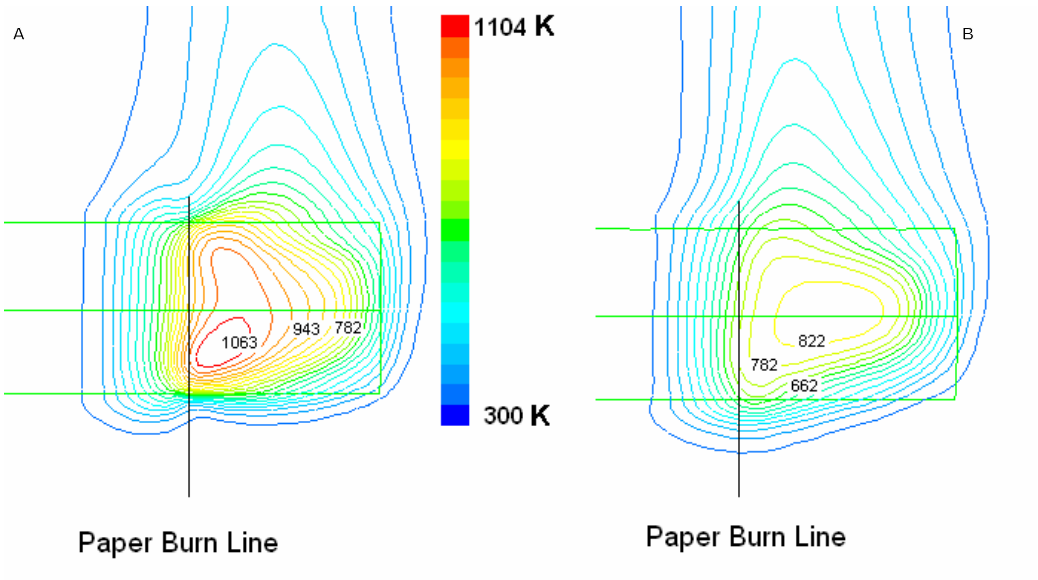

Figure 2. Numerical results of gas temperature contours at (A) 1 s after start of a puff, (B) 3 s into smoldering

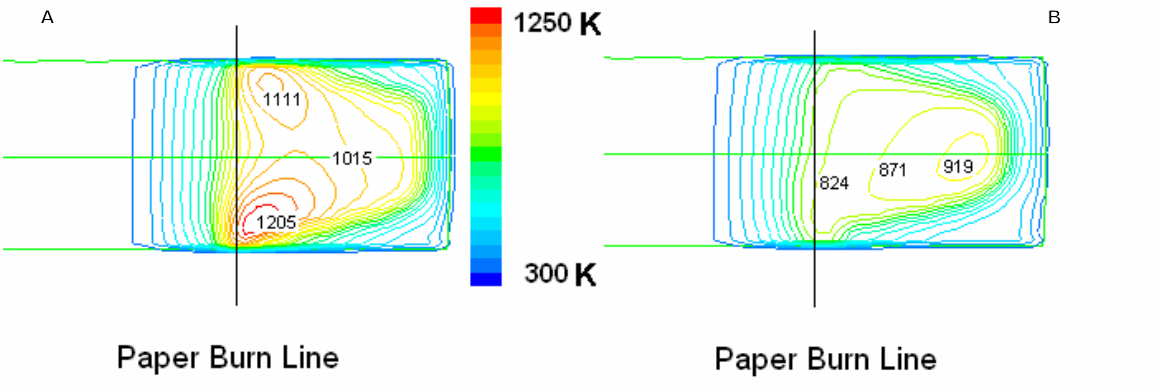

Figure 3. Numerical results of solid temperature contours at (A) 1 s after start of a puff, (B) 3 s into smoldering

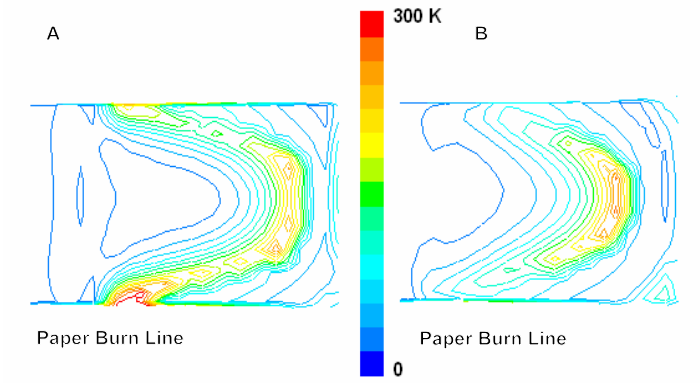

Figure 4. Numerical results of contours of $|T_s - T_g|$ (K) during (A) puffing and (B) smoldering

center of the coal during smoldering rather than at the periphery of the coal as seen at the peak of the puff. The experimental results show that the higher burn rate on the lower surface of horizontally burned cigarette, which is the common orientation for smoking a cigarette, causes the paper burn-line not to be vertical but slightly tilted. This behavior is reproduced by the model and is clearly noticed in Figure 3b.

During puffing the rate of heat production is almost six times higher than during smoldering. This causes the solid and gas temperatures to be higher during puffing. It is believed that high heating rates and high local gas velocities do not allow the solid and gas temperatures to reach a thermal equilibrium. In order to find the extent of non-equilibrium, the absolute difference between solid and gas temperatures at the peak of the puff and during smoldering were calculated and are shown in Figures 4a and 4b. It can be noticed that the maximum difference of about 300 K is observed during puffing. Even during smoldering a considerable temperature difference is noted, indicating

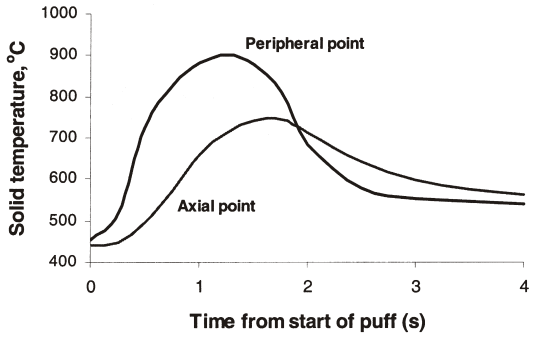

Figure 5. Numerical results of the time variation of tobacco axial and peripheral particles during puffing and smoldering

Figure 6 shows the char density contours at a) the peak of the puff (1 s after the start of the puff) and b) smoldering, i.e. 3 s after the end of the puff. The contours at both the instances are similar in the coal region; however there is a reduction in the size for the case of smoldering. Also note the higher char density along the periphery near the paper burn-line at the peak of the puff. This is the new char produced due to oxidation caused by inflow of fresh air while drawing the puff. As the smoldering progresses into time, this peripheral region shrinks and joins with the forward moving main coal region, as can be seen from the Figure 6b.

Figures 7a and 7b show the contours of CO mass fraction on the plane passing through the center of the cigarette at 1 s after the start of puffing and 3 s after the end of puffing (i.e., during smoldering), respectively. Maximum amount of CO is seen in

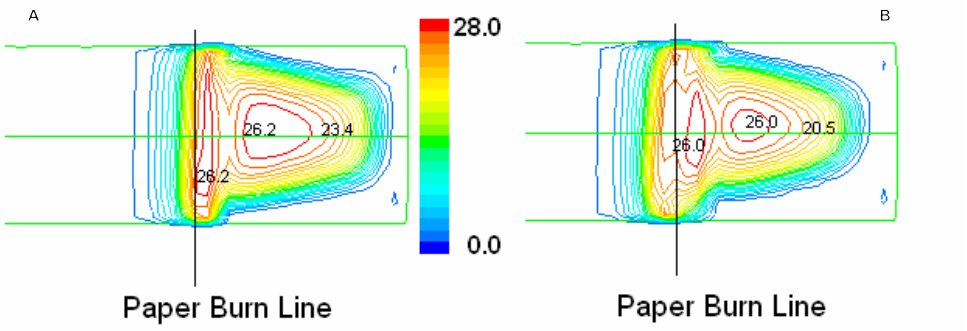

Figure 6. Numerical results of char density (kg/m^3) contours at (A) 1 s after start of a puff, (B) 3 s into smoldering

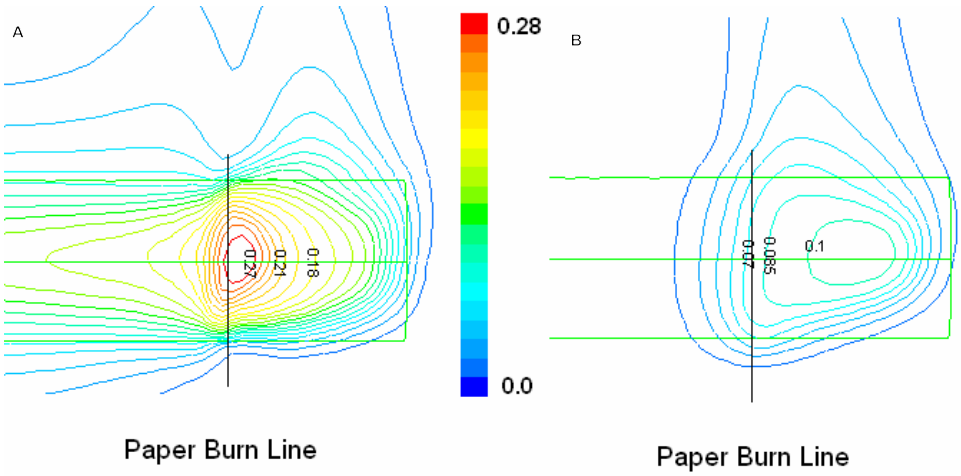

Figure 7. Numerical results of CO mass fraction contours at (A) 1 s after start of a puff, (B) 3 s into smoldering

thermal non-equilibrium between these two phases. The temperature difference is low only in the central part of the coal, where the gas velocity is very low for smoldering and puffing. Therefore treating solid and gas energy equations separately is the proper choice for this problem.

The heat propagation through the tobacco column is shown by tracing the temperature change of a fixed tobacco particle. We consider two tobacco particles; one positioned on the cigarette axis and one on the periphery and on a line passing through the paper burn-line as we start the puff. Figure 5 shows that both particles experience a sharp change in their temperature rising to 1013 K (740 ˚C) and 1193 K (920 ˚C) and with heating rates as high as 300 and 500 K/s.

the coal region just in front of the paper burn-line. Most of the CO produced passes along the tobacco column in the main-stream smoke due to the draw during puffing. As it passes along the tobacco column, CO diffuses out from the paper, which is clearly seen from Figure 7a. However during smoldering, most of the CO generated is contained in the near coal region and almost all of this CO generated will flow into the sidestream smoke. Figures 8a and 8b show the contours of velocity magnitude on the plane passing through the center of the cigarette at peak of the puff (1 s after puffing starts) and 3 s after the end of puffing (smoldering), respectively. Most of the air flowing into the tobacco column enters in along the periphery of the cigarette where the paper has just burnt. This

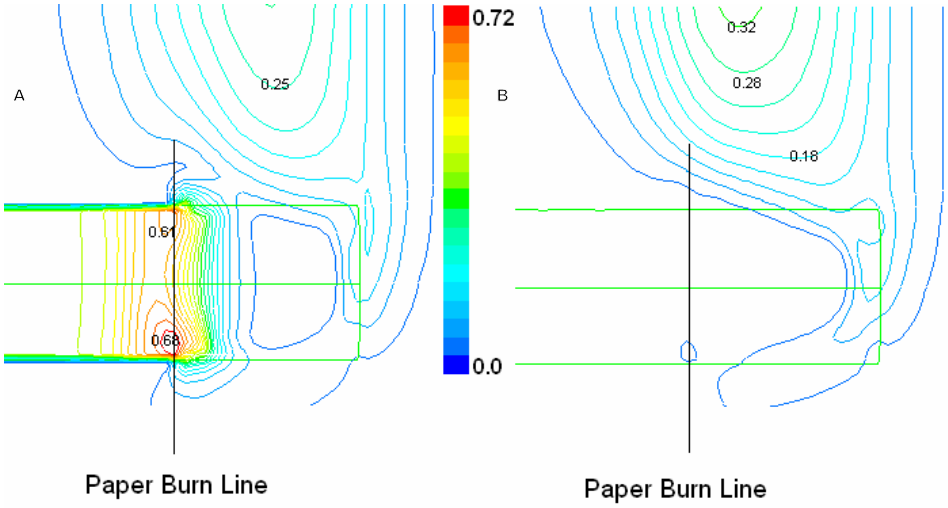

Figure 8. Numerical results of velocity magnitude (m/s) contours at (A) 1 s after start of a puff, (B) 3 s into smoldering

Table 3. Some experimental and numerical data on smoldering and puffing

	Smoldering		Puffing	
Parameters	Experimental	Numerical	Experimental	Numerical
Mass burn rate (mg/s)	0.92	0.96	5.9	6.1
Max solid temperature (˚C)	775	720	950	960
Max gas temperature (˚C)	775	600	850	780

is indicated by the red circular contours just beneath the paper. Figure 8b shows the velocity contours during smoldering on the plane passing through the center of the cigarette. It is interesting to note that not only the velocity contours for sidestream smoke are the same during both puffing and smoldering but also even their magnitudes are similar. In order to validate the mathematical model, the maximum solid and gas temperatures and also the average mass burn rates during smoldering and puffing are compared with experimental results as depicted in Table 3. It can be noted that the numerical results are in a very good agreement with the experimental results of a typical cigarette. BAKER (40) has measured the gas and solid temperature contours of a puffing cigarette. Since the data correspond to a horizontal plane passing through the cigarette axis, here we also obtained data numerically on the same plane. The results corresponding to the peak of the puff are shown in Figure 9. Given the fact that the tobacco blend of the numerical model and the experimental one are not the same, it can be noted that the model has reproduced the basic features of the temperature distribution, and the numerical results are quantitatively in good agreement with the experimental results.

The mainstream smoke constituents are measured for different cigarette brands. In order to compare the smoke constituents' yields with experimental results, the mass flow rate of each component at the cigarette outlet was integrated during the 2-second puff and depicted in Table 4. Comparison shows for most of the components that there is good agreement between experimental and numerical results. In this simulation, the formation, adsorption and transport of aerosol particles through the cigarette column is not modeled and consequently the water vapor condensation into aerosol particles are not modeled either. This has caused more deviation between the esults for particulate phase and water vapor. Also, we have neither modeled the homogeneous gaseous reactions during char oxidation nor have we considered the catalytic effect of water vapor and alkaline metals in CO/CO_2 formation. These factors have considerable effect on the concentration of CO and CO_2 in mainstream smoke. We should add to this the fact that the pyrolysis experiments are normally performed under conditions of heating rates and residence times, which are different from the conditions inside a burning cigarette. The temperature and velocity of smoke plume on a line one centimeter above the coal of a smoldering cigarette has been calculated and is compared with the measured data in Figure 10. A good agreement between numerical and experimental temperature values is observed on this line. However, the numerical results of velocity are comparatively lower than the experimental ones. The main reason is that the temperatures in the coal region predicted by the model during smolder are lower than the measured data. Analysis of the data shows that the coal is overcooled by the effect of radiation, and, replacing the simple coal-cooling model by a more rigorous one should improve the results.

The intra-puff delivery pattern of CO, CO_2, and H_2O for a 2 s, 35 cc sinusoidal puff is depicted in Figure 11. All three gases follow a trend similar to puff mass flow rate, but with a time delay, which is larger for CO and CO_2 and relatively shorter for H_2O. During smoldering the gaseous species concentration is nonzero inside the cigarette coal and in the smoke plume. As the puffing starts, the flow velocity at the filter end gradually increases (because of sinusoidal profile)

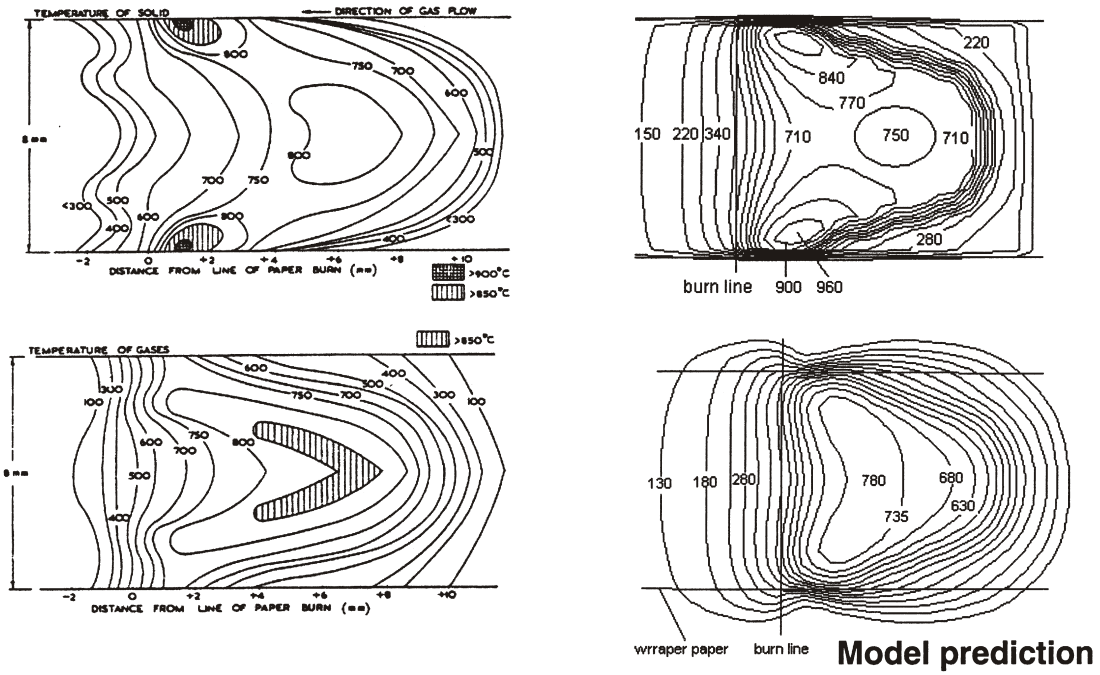

Figure 9. Contours of solid and gas temperatures on a horizontal plane passing through the cigarette axis (˚C); reprinted from *High Temperature Science* 1975 (7) 236–247

Table 4. Some experimental and numerical data on mainstream smoke constituents' yields of an unfiltered cigarette

Data	Oxygen	Carbon dioxide	Carbon monoxide	Vapor phase	Particulate phase	Nitrogen	
Comparison with a given brand (weight%/cigarette)							
Experimental	13	12.5	4	4	4.5	62	
Numerical	12	13	4	5	8	58	
Data	Oxygen	Carbon dioxide	Carbon monoxide	Nitrogen	Water vapor	Acetaldehyde	Nicotine
Comparison with a range of cigarettes (mg/cigarette)							
Min. experimental	70	50	23	320	14	1.2	2.3
Numerical	68.9	36.4	15.7	293	17.8	1.1	1.4
Max. experimental	50	20	10	280	3	0.5	0.8

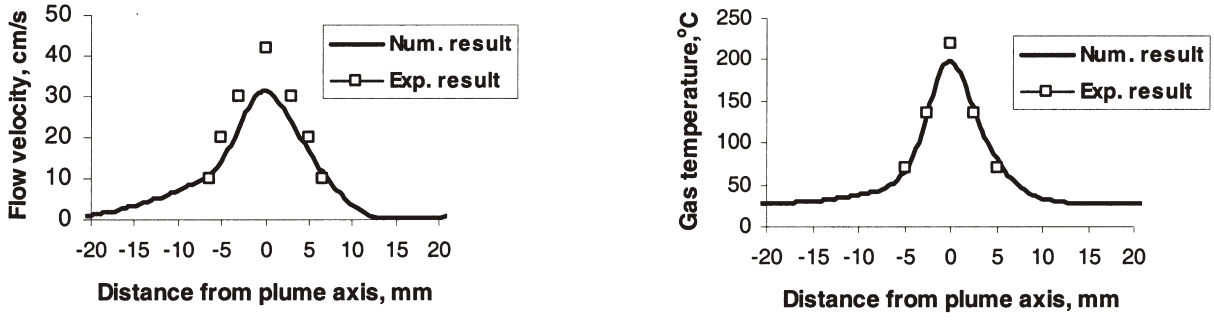

Figure 10. Numerical results of gas temperature and velocity in smoke plume during smoldering

and thus it takes about 0.4 s for the gaseous species to travel from the coal region to the outlet. However, the situation is slightly different for H_2O. This is because H_2O vapor is not only generated from tobacco pyrolysis but also from moisture evaporation. Evaporation takes place at lower temperatures and in the tobacco column behind the coal region, which is closer to the filter end. Thus water vapor production starts sooner and nearer to the filter end

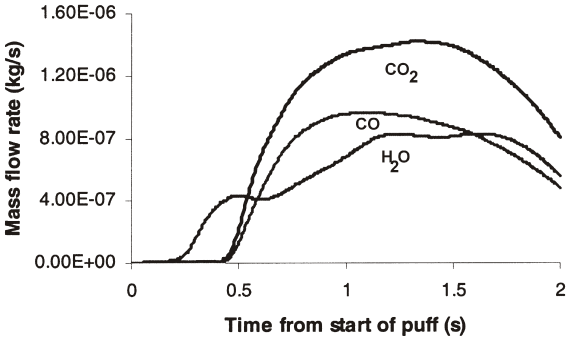

Figure 11. Numerical results of CO, CO_2, and H_2O profiles

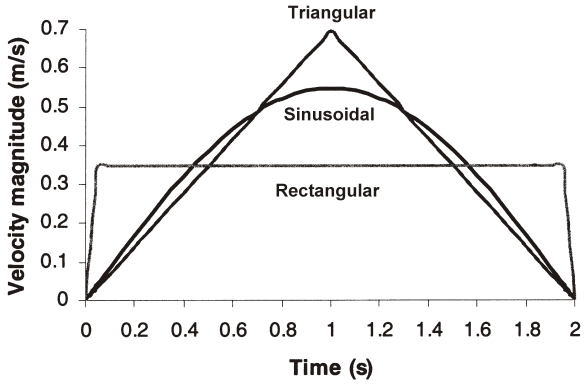

Figure 12. Velocity profile at the cigarette outlet for various puff profiles

than CO and CO_2, which are generated due to pyrolysis and char oxidation at higher temperatures and their evolution is confined only to the coal region. Therefore H_2O is delivered at the outlet with a shorter time delay. As soon as the solid temperature rises enough to produce CO and CO_2, carrier gases deliver these gases at the outlet, nevertheless with a larger time delay. Rapid increase of CO and CO_2 at the outlet decreases the mass fraction of H_2O at the outlet momentarily. However, once production of H_2O starts due to pyrolysis, all of the above components show a consistent increasing trend until the mass flow rate decline due to the sinusoidal puff profile, which affects the production and delivery of the three components.

Effect of puff profile and puff duration

Three different puff profiles, which are commonly used in the industry to incorporate the variation in individual smoking pattern, are employed in our present analysis and their effect on mass burn rate, temperature and smoke chemistry is studied. Figure 12 shows the velocity profile for the various puffs, i.e. sinusoidal, triangular and rectangular puffs. All three puff profiles draw an equal amount of puff volume of 35 cc in a 2 s time period. Figure 13 shows the effect of the puff profile on the mass burn rate (mg/s) during the 2-second puffing period. A strong similarity can be clearly noticed between the mass burn rate profile and the velocity profile except during the start and end of the puff. The mass burn rates for the sinusoidal (base) and triangular case are similar because of the similarity in their velocity profiles. Even though there is a

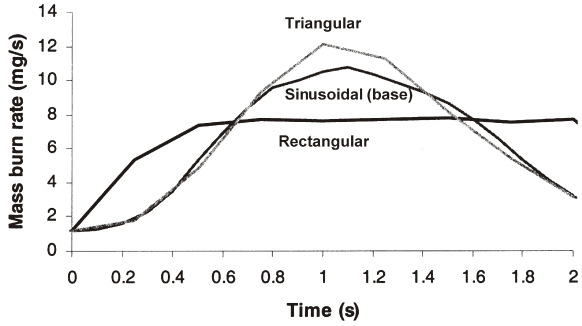

Figure 13. Effect of puff profile on mass burn rate during puffing

Table 5. Results of different puff profiles for 2 second puffs

Puff profile	Sinusoidal	Triangular	Rectangular
Puff volume (cc)	35	35	35
T_s (˚C)	919.6	942.2	850.8
T_g max (˚C)	796.6	804.7	761.4
Mass burn rate (mg/puff)	13.8	14.5	15.3
MS CO_2 delivery (mg)	2.6	2.5	2.6
MS CO delivery (mg)	1.1	1.1	1.1
MS H_2O delivery (mg)	0.5	0.5	0.5
MS O_2 delivery (mg)	7.7	7.7	7.7

sudden jump in the velocity magnitude for the rectangular case, it takes a while for the mass burn rate to reach a steady state. There is a gradual increase in the mass burn rate until 0.4 s and it remains fairly constant there after.

Table 5 shows a comparison between the three puff profiles. The maximum solid and gas temperatures obtained during the 2-second puff are highest for triangular followed by sinusoidal and then rectangular. The solid temperature and consequently the gas temperature are affected by the inflow of air at paper burn-line, which varies with the outlet velocity. For the triangular profile we have the highest outlet velocity followed by sinusoidal and rectangular profiles. As we expect, the same trend is observed in Table 5 for solid and gas temperatures. The mass burn rate for the rectangular profile is slightly higher than the triangular profile followed by the sinusoidal profile. The mass burn rate is the combination of mass lost during pyrolysis and char oxidation. The rate of pyrolysis is a function of solid temperature and it changes drastically for temperatures less than 700 K (427 ˚C), but for higher solid temperatures it increases slightly. On the other hand, the char oxidation is mainly a mass transfer control process and it is more sensitive to flow velocity than to solid temperature. For the rectangular profile the solid temperature is fairly high for most of the period of the puff causing higher mass burnt due to pyrolysis and char consumption. The mass burn rate is affected depending on the contribution and amount of each of the above-mentioned processes. Table 5 indicates that for the rectangular profile, the higher pyrolysis rate has caused the mass burn rate to be higher while for the triangular profile the higher char oxidation is the main reason for higher mass burn rate. Table 5 shows that the mainstream smoke delivery is not sensitive to the puff profile. The smoke delivery not only depends on the

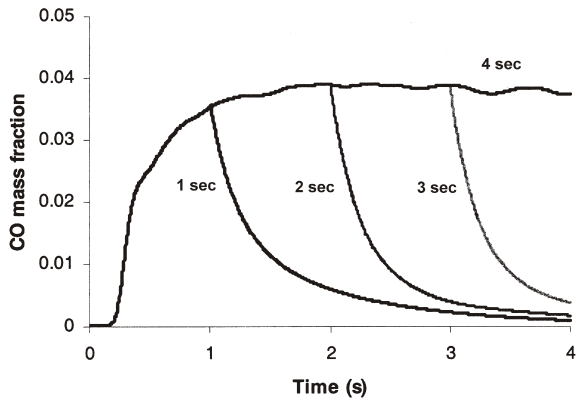

Figure 14. Effect of puff duration on average mass fraction of CO at the end of a cigarette filter for a rectangular puff profile

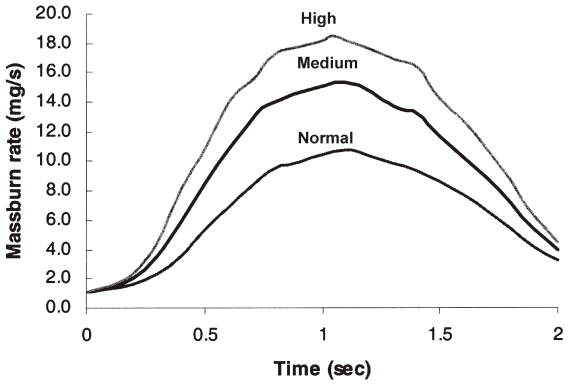

Figure 15. Effect of puff standards on mass burn rate during a 2 s puff

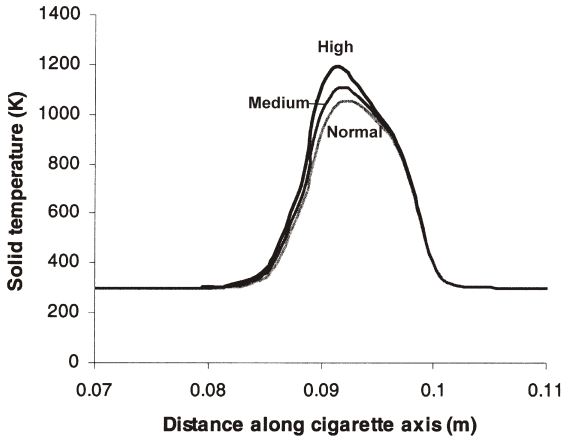

Figure 16. Numerical results for the effects of different puff intensities on solid temperature along the cigarette centerline 1 s after start of the second puff

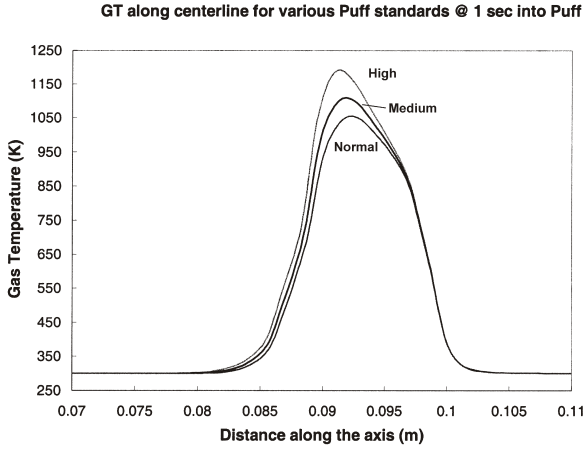

Figure 17. Numerical results for the effects of different puff intensities on gas temperature along the cigarette centerline 1 s after start of the second puff

production rate of gaseous species but also depends on the rate of gaseous dilution in the cigarette column. The production rate is proportional to the mass burn rate and should be highest for the rectangular profile. On the other hand, for the rectangular profile we have a shorter delay in delivery of smoke constituents. Also since the flow velocity and gaseous species concentration through the tobacco column is a function of puff profile; we expect to have different rates of dilution for different profiles. All these counteracting effects have caused the total delivery of smoke constituents to be the same for the three profiles.

Figure 14 shows the effect of puff duration on the average mass fraction of CO_2 on the outlet. The results are shown for four puffs with duration of 1, 2, 3 and 4 s each and having the rectangular puff profile. It can be noticed that the mass fraction of CO_2 increases until 1.75 s and remains constant there after for the 3 s and 4 s long puffs. As the puff mass flow rate is kept constant, the puffing behavior approaches a quasi steady state in about one and half seconds.

Puff intensity

The three puffing intensities used are as follows: 1) Normal which has 35 cc flow rate with all the ventilation holes kept open, 2) medium with 45 cc flow rates and half the ventilation holes blocked, and 3) high with 55 cc flow rate and all ventilation holes blocked. All three standards have a sinusoidal puff profile and all other conditions are kept constant. Figure 15 shows the variation in mass burn rate during puffing for different puff intensities. Mass burn rate for all three profiles is similar to their velocity profile, which is sinusoidal and is highest for high intensity puff followed by medium intensity and then normal puff. The mass burn rate is directly proportional to the flow rate and inversely proportional to the ventilation effect. Figures 16 and 17 show solid and gas temperatures along the cigarette axis for three puff intensities. It is clearly seen that high intensity puffs have higher solid and gas temperatures in the coal region followed by the medium and then normal. Also, the peak for the high intensity puff has relatively moved leftwards indicating that the paper burn-line has moved more into the cigarette compared to medium and normal intensity puffs. This is attributed to the higher flow rate and no ventilation, forcing a larger amount of air to enter into the tobacco column through the periphery near the paper burn-line region, and therefore a longer coal region and higher temperatures. This effect is more clearly understood by looking at the solid temperatures along the axis of the cigarette in the coal region. The solid temperature is higher for the higher flow rate. The peaks

Table 6. Results of different puff intensities for 2-second puffs

Puff intensity	Normal	Medium	High
Puff volume (cc)	35	45	55
Ventilation (%)	All holes open	Half holes closed	All holes closed
$T_{s,}$ max (˚C)	920	980	1161
$T_{g,}$ max (˚C)	797	862	1049
Mass burn rate (mg/puff)	13.4	18.9	23.3
Combustion heat (W/puff)	25.8	29.9	39.2
MS CO_2 delivery (mg)	2.6	3.4	4.06
MS CO delivery (mg)	1.1	1.4	1.6
MS H_2O delivery (mg)	0.5	0.6	0.7
MS O_2 delivery (mg)	7.7	6.9	6.2

Table 7. Results of puff-by-puff simulation for 2-second puffs

Puff number	2	4	6	8
$T_{s,}$ max (˚C)	920	947	968	997
$T_{g,}$ max (˚C)	797	818	845	859
Mass burn rate (mg/puff)	13.4	14.5	15.3	16.1
MS CO_2 delivery (mg)	2.6	3.2	4.3	5.1
MS CO delivery (mg)	1.1	1.3	1.6	1.9
MS H_2O delivery (mg)	0.5	0.6	0.6	0.6
MS O_2 delivery (mg)	7.7	7.1	6.4	5.7

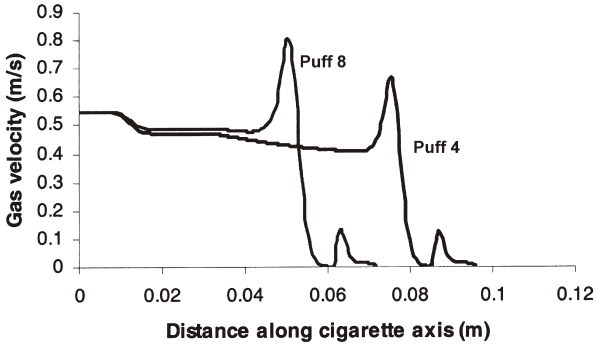

Figure 18. Numerical results of the velocity profile along the cigarette axis 1 s after start of puffs 4 and 8

indicting the location of the paper burn-line are more distinctly visible for the solid temperature case. The sudden decrease in temperature near the vertex of the conical shaped coal implies that the tobacco has burnt completely and only ash is left over beyond that point.

Table 6 quantitatively compares the salient features of three puff intensities. It can be clearly seen from the table that a higher flow rate induces higher solid and gas temperatures, with highest being for high and lowest for normal intensity puffs. Also, the mass burn rate is higher for high, then for medium and lowest for the normal intensity. The amount of draw is directly and that of ventilation inversely proportional to the mainstream components of volatiles and gases generated at the coal. Therefore, the mainstream concentration of CO_2, CO and H_2O is highest for high intensity with 55 cc, 2 s flow rate and 0% ventilation followed by medium and finally lowest for normal intensity (35 cc and all vent holes kept open).

Simulation of puff-by-puff

Table 7 shows the maximum solid and gas temperatures attained and the amount of mainstream components during the two-second puffing period with a sinusoidal profile for puffs 2, 4, 6 and 8. The maximum solid and gas temperature attained during the 2 s puff increases by puff number. In standard practice, each puff cycle accounts for 2 s of puffing followed by 58 s of smoldering and results in a decrease in the tobacco column by about 5 mm. Therefore with an increase in puff count, the tobacco column decreases. Since the puff volume remains the same and the tobacco column length decreases, less air enters into the column through the paper and more air flows in through the periphery of the cigarette near the paper burn-line. This leads to less dilution of smoke gaseous species with an increase in puff number. More amount of air entering through the coal region is responsible for the higher gas and solid temperatures, higher linear and mass burn rates, and higher amount of mainstream smoke components.

The distribution of some of the flow quantities and gaseous products along the cigarette axis corresponding to the peak of the puff are studied in Figures 18 through 23. For comparison here only the results corresponding to puffs 4 and 8 are presented. In all of the following figures, the general trend is that puff 8 has comparatively higher gas velocity, temperature and gaseous products.

Figure 18 shows the gas velocity magnitude along the cigarette axis. The large peak represents the vicinity of the paper burn-line where the inflow of air and the production of gases due to combustion is maximum. The hot gases expand rapidly resulting in comparatively high flow velocities. During puffing and smoldering, since the heat front and paper burn-line move into the tobacco column, the peak of puff 8 locates closer to the cigarette filter end. The smaller peak in the front is due to the flow induced by buoyancy forces around the cigarette coal. The peak specifically represents the flow passing by the coal tip and moving upward. The velocity magnitude falls down rapidly on either side of the paper burn-line. The decrease in magnitude on the coal side is partly because of the decrease in gas temperature and partly because of high resistance offered to flow in the coal zone. The decrease in velocity magnitude on the tobacco side is attributed to the steep decrease in gas temperature in this region. The velocity magnitude gradually increases after the sudden drop due to

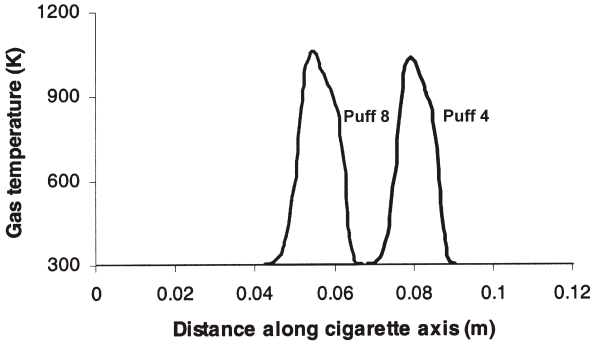

Figure 19. Numerical results for the gas temperature profile along the cigarette axis 1 s after start of puffs 4 and 8

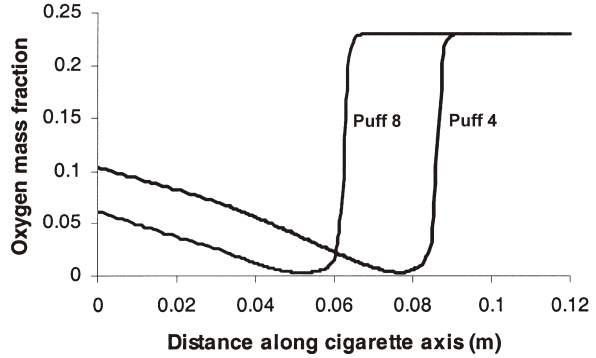

Figure 20. Numerical results for oxygen (O_2) concentration (mass fraction) along the cigarette axis 1 s after start of puffs 4 and 8

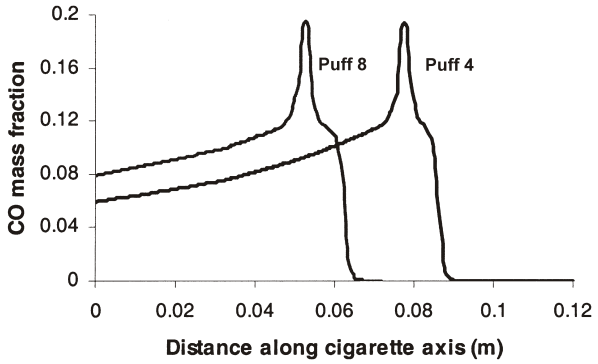

Figure 21. Numerical results for carbon monoxide (CO) concentration (mass fraction) along the cigarette axis 1 s after start of puffs 4 and 8

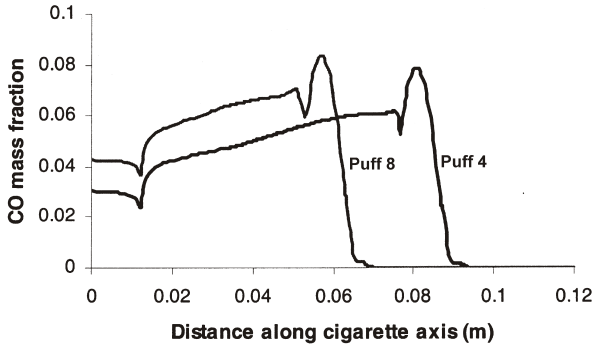

Figure 22. Numerical results for CO concentration (mass fraction) along the cigarette upper surface 1 s after start of puffs 4 and 8

inflow of air through the wrapper paper till it reaches the filter. Since the tipping paper used for the filter is impermeable, the flow velocity remains fairly constant. A sudden but small increase in velocity in the filter is due to the inflow of small amount of air through the ventilation holes. Figure 19 shows the variation in gas temperature along the axis of the cigarette, in the coal region, for puffs 4 and 8. The gas temperature is highest near the paper burn-line and decreases on either side of the paper burn-line. The decrease in gas temperature in the coal region is less steep because of the heat generation due to char oxidation. On the other hand the fall in gas temperature is very rapid in the tobacco column. The heat capacity of the tobacco shreds is almost 1000 times larger than that of the hot gases. Also, the solid-gas interfacial surface area per unit volume is very large behind the paper burn-line; the hot gas loses its energy very quickly to the cool solid material in a few millimeters distance while passing through the tobacco column. Therefore, a steep decline in gas temperature can be observed on the filter end in the tobacco column.

Figure 20 shows the oxygen mass fraction on the axis of the cigarette at 1 s after the start of the puff. Since the rate of oxygen consumption and production of gaseous species is higher in puff no. 8 than compared to puff 4, the oxygen concentration along the cigarette axis is lower for puff no. 8. It can be noticed from the plot that the coal region is mainly an oxygen deficient zone where the oxygen mass fraction depletes to almost zero. In the downstream side in the tobacco column the oxygen concentration increases due to inflow of air and also due to diffusion of oxygen through the wrapper paper.

Figure 21 shows the mass fraction of CO along the axis of the cigarette at 1 s after the start of the puff for puffs 4 and 8. The simulation results show a distinct peak at the burn-line with a very steep decline on the both sides. Even though CO is produced by both pyrolysis and char oxidation, the contribution of char oxidation in CO production is much more significant. Thus, it is expected to see a lower rate of decline in CO concentration from the peak toward the coal as compared to the opposite site toward the filter. The shoulder of the peak on the coal side represents the production of CO within the coal due to char oxidation. As the gases move along the tobacco column towards the filter, CO concentration decreases due to the dilution of CO caused by inflow of air into the column and outward diffusion of CO through the wrapper paper.

Figure 22 shows the distribution of CO on the upper surface of the cigarette. The peak corresponds to the sidestream smoke plume that evolves CO from the coal region due to buoyancy and increases CO concentration of the surrounding air. A sudden and steep dip in the CO mass fraction can be observed next to the peak. This dip represents the location of the paper burn-line where the surrounding air is brought into the tobacco column, lowering the concentration of CO in that region. Immediately behind this dip the concentration of CO rapidly increases due to diffusion of CO from the wrapper

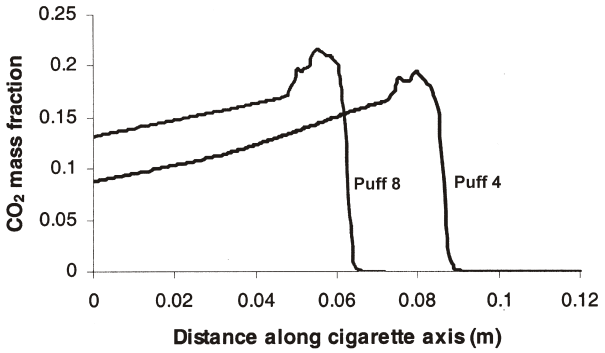

Figure 23. Numerical results for CO_2 concentration (mass fraction) along the cigarette axis at 1 s after start of puffs 4 and 8

paper of the tobacco column into ambient air. The CO concentration decreases afterwards because further dilution of CO in the tobacco column. Finally, another dip in the CO concentration can be observed in the filter region at the location of ventilation holes. It is interesting to note that a similar kind of dip is not seen in Figures 20 and 21, where the concentration of CO and O_2 is plotted on the axis of the cigarette. The main reason is that the transport of gaseous species in the tobacco column is primarily a convective mechanism and diffusion plays only a secondary role. The convective mechanism makes the concentration to be affected by the upstream values. Thus except for the points in the vicinity of the ventilation, the presence of ventilation affects the CO concentration at points located down stream of ventilation location.

Figure 23 shows the CO_2 concentration along the axis of the cigarette at 1 s after the start of the puff. It is interesting to note the two distinct peaks in the coal region of the cigarette. The higher peak corresponds to CO_2 production due to char oxidation and the lower one, located behind the paper burn-line in the tobacco column, is due to the pyrolysis of tobacco. Unlike CO, the rate of CO_2 production from pyrolysis is significant. The average value of CO_2 to CO ratio (CO_2/CO) due to pyrolysis is as high as 6, explaining the presence of a second peak in CO_2 concentration.

CONCLUSION

For the first time, a 3-D model was successfully developed that numerically simulates the puff-smoldering cycle of a lit-end cigarette. The solid- and gas-phase temperatures as well as mainstream smoke constituents predicted by the model for a puffing cigarette are in a good agreement with experimental results. A parametric study shows the significant effect of puff volume, puff profile, ventilation rate, and puff number on solid and gas phase temperatures as well as gaseous species concentrations and mainstream smoke delivery. Further, it is shown that buoyancy forces have an important role in both smoldering and puffing, and in order to get more realistic results, they have to be included in the model. The variation of gas and solid properties and also the gaseous species along the surface of the cigarette show that inclusion of surrounding air in the computational domain is justified rather than setting boundary conditions on the cigarette surface. And finally it was shown that during puffing the difference between solid- and gas-phase temperatures are too large for considering models based on thermal equilibrium between two phases.

NOMENCLATURE

A_i (s^{-1})	Pre-exponent factor of the i^{th} precursor of tobacco pyrolysis Pre-exponent factor of the i^{th} precursor of char oxidation
A_v (m^{-1})	Surface to volume ratio of tobacco column
A_{we} (s^{-1})	Pre-exponent factor of moisture evaporation
A_{vt} (m^{-1})	Surface to volume ratio of for coal radiation cooling
A_{ash} (m^{-1})	Surface to volume ratio of coal ash
C_{pg} (kJ/kg·K)	Gas average specific heat
C_{ps} (kJ/kg·K)	Tobacco shred specific heat
D_p (m)	Tobacco column equivalent spherical particle average diameter
D_{gi} (m^2/s)	Mass diffusion coefficient of the gas i^{th} component
$\boldsymbol{D}_t^d$ (m^2/s)	Thermal dispersion coefficient
$\boldsymbol{D}_m^d$ (m^2/s)	Mass dispersion coefficient
D_{AB} (m^2/s)	Mass diffusion coefficient of a binary gas mixture in a porous media
d_{AB} (m^2/s)	Mass diffusion coefficient of a binary gas mixture
E_{01} (kJ/mol·K)	Activation energy of the i^{th} precursor of tobacco pyrolysis Activation energy of the i^{th} precursor of char oxidation
E_{we} (kJ/mol·K)	Activation energy of moisture evaporation
f_{rad}	Coal radiation cooling position factor
h (W/m^2/K)	Tobacco shreds-gas heat transfer coefficient
h_m (m/s)	Tobacco shreds-gas mass transfer coefficient
$H_{combustion}$ (J/kg)	Char oxidation heat production
$H_{pyrolysis}$ (J/kg)	Tobacco pyrolysis heat consumption
$H_{evaporation}$ (J/kg)	Tobacco moisture evaporation heat consumption
$H_{lighter}$ (W/m^3)	Lighter heat production rate
K_i (s^{-1})	Kinetic constant of the i^{th} precursor of tobacco pyrolysis
K_{we} (s^{-1})	Kinetic constant of the moisture evaporation
k_g (W/m·K)	Gas thermal conductivity
k_s (W/m·K)	Tobacco shred thermal conductivity
k_{seff} (W/m·K)	Tobacco column solid phase effective thermal conductivity
k_{geff} (W/m·K)	Tobacco column gas phase effective thermal conductivity
k_r (W/m·K)	Tobacco column effective radiation conductivity
K (m^2)	Tobacco column permeability
$\mathbf{Nu} = \frac{h\boldsymbol{D}_p}{\boldsymbol{k}_g}$	Nusselt number

P (Pa)	Pressure
$\mathrm{Pr} = \nu_g/\alpha_t$	Prandtl number
$\mathbf{Re} = \frac{\bar{u}D_p}{\nu_g}$	Reynolds number
$\mathbf{Sh} = \frac{h_m D_p}{\alpha_m}$	Sherwood number
$\mathbf{Sc} = \frac{\nu_g}{\alpha_m}$	Schmit number
T_g (K)	Gas temperature
T_s (K)	Solid temperature
T_∞ (K)	Ambient temperature
T_p (K)	Sinusoidal puff period
$\vec{V}$ (m/s)	Superficial velocity
V_i^*	Maximum yield of the i^{th} precursor of tobacco pyrolysis
V_i^n	Yield of the i^{th} precursor of tobacco pyrolysis at time t_n
V_{ci}	Ratio of the i^{th} precursor of char oxidation
V_{max} (m/s)	Maximum velocity of the sinusoidal puff profile
Y_i	Mass fraction of the smoke i^{th} component
$Y_{O_2}^n$	Mass fraction of oxygen at time t_n

Greek symbols:

ρ_g (kg/m^3)	Gas density
ρ_s (kg/m^3)	Tobacco shred density
ρ_{we} (kg/m^3)	Tobacco shred moisture density
ρ_{daf} (kg/m^3)	Tobacco shred dry-ash-free density
$\rho_{char,k}$ (kg/m^3)	Kinetic controlled char oxidation density
$\rho_{char,m}$ (kg/m^3)	Mass transfer controlled char oxidation density
ρ_{char} (kg/m^3)	Char density
ρ_{py} (kg/m^3)	Tobacco pyrolysis density
ρ_{CO} (kg/m^3)	CO density due to char oxidation
ρ_{CO2} (kg/m^3)	CO_2 density due to char oxidation
ρ_{O2} (kg/m^3)	Oxygen density
ρ_{ash} (kg/m^3)	Ash density
ρ_b (kg/m^3)	Porous media density
ν_g (m^2/s)	Gas kinematic viscosity
α_t (m^2/s)	Gas thermal diffusivity
α_m (m^2/s)	Gas mass diffusivity
μ (kg/m·s)	Gas dynamic viscosity
σ (W/m^2·K^4)	Stefan-Boltzmann constant
σ_i	Standard deviation of the i^{th} precursor of tobacco pyrolysis
ε	Emmisivity
Φ	Tobacco column porosity

ACKNOWLEDGEMENT

Authors would like to thank Dr. F. Rasouli for his technical assistance and discussions, and Drs. P. Chen, P. Lipowicz, and C. Lilly for their helpful comments. Saidi Partnership would also like to acknowledge Philip Morris USA, Inc. for the financial support, and Isfahan University of Technology for extending Dr. Saidi's sabbatical.

REFERENCES

1. Egerton, A., K. Gugan, and F.J. Weinberg: The mechanism of smoldering in cigarettes; Combust. Flame 7 (1963) 63–78.
2. Ohlemiller, T. J.: Modeling of smoldering combustion propagation; Prog. Energy Combustion Sci. 11 (1985) 277–310.
3. Summerfield, A.M., T.J. Ohlemiller, and H.W. Sandusky: A thermo-physical mathematical model of steady-draw smoking and predictions of overall cigarette behavior; Combust. Flame 33 (1973) 263–279.
4. Norbury, J., and M.A. Stuart: A model for porous-medium combustion; Q. J. Mechanics Appl. Math. 42 (1989) 159–178.
5. Kansa, E.J., H.E. Perlee, and R.F. Chaiken: Mathematical model of wood pyrolysis including internal forced convection; Combust. Flame 29 (1977) 311–324.
6. Leach, S.V., G. Rein, J.L. Ellzey, O.A. Ezekoye, and J.L. Torero: Kinetic and fuel property effects on forward smoldering; Combust. Flame 120 (2000) 346–358.
7. Muramatsu, M., S. Umemura, and T. Okada: A mathematical model of evaporation-pyrolysis processes inside a naturally smoldering cigarette; Combust Flame 36 (1979) 245–262.
8. Sandusky, H.W.: A computer-simulated cigarette model for use in the development of less hazardous cigarette; Ph.D. Thesis, 1976, Princeton University, Princeton, NJ.
9. Di Blasi, D.C.: Modeling and simulation of combustion processes of charring and non-charring solid fuels; Prog. Energy Combust. Sci. 19 (1993) 71–104.
10. Yi, S., E. Song and M.R. Hajaligol: Mathematical model of smoldering combustion in a carbonaceous porous medium, Part 1- Development of pyrolysis and combustion models for a cylindrical geometry; J. Fire Sciences 19 (2001) 429–448.
11. Rostami, A., J. Murthy, and M.R. Hajaligol: Modeling of a smoldering cigarette; J. Anal. Appl. Pyrolysis 66 (2003) 281–301.
12. Rostami, A., J. Murthy, and M.R. Hajaligol: Modeling of the smoldering process in a porous biomass fuel rod; Fuel 83 (2004) 1527–1536.
13. Saidi, M.S., M.R. Hajaligol, and F. Rasouli: An experimental and numerical analysis of puff hydrodynamics; Beitr. Tabakfosch. Int. 21 (2004) 157–166.
14. Saidi, M.S., M.R. Hajaligol, and F. Rasouli: Numerical simulation of a burning cigarette during puffing; J. Anal. Appl. Pyrolysis 72 (2004) 141–152.
15. Baker, R.R.: The kinetics of tobacco pyrolysis, Thermochim. Acta 17 (1976) 29–63.
16. M.A. Wojtowicz, R. Bassilakis, W.W. Smith, Y. Chen and R.M. Carangelo: Modeling the evolution of volatile species during tobacco pyrolysis, J. Anal. Appl. Pyrolysis 66 (2003) 235–261.
17. Suuberg, E.M.: Approximate solution technique for non-isothermal, Gaussian distributed activation energy models; Combust. Flame 50 (1983) 243–245.

18. Du, Z., A.F. Sarofim, J.P. Longwell, and L. Tognotti: The CO/CO_2 ratio in the products of the carbon-oxygen reaction, Fundamental issues in control of carbon gasification reactivity; Kluwer Academic Publishers, Netherlands 1991, pp. 91–196.
19. Muramatsu, M., S. Umemura, and T. Okada: Consumption of oxygen and heat evolved during natural smolder of a cigarette; J. Chem. Soc. Japan, Chem. and Ind. Chem. (1978) 1441–1448.
20. Ergun, S.: Fluid flow transport through packed column; Chem. Eng. Prog. 48 (1952) 89–94.
21. Dullien, F.A.L.: Porous media: fluid transport and pore structure; second edition, Academic Press, 1992.
22. Perry, R.H. and D.W. Green: Perry's Chemical Engineers' Hand Book; seventh edition, McGraw Hill, N.Y., 1997.
23. Fatehi, M. and M. Kaviany: Role of gas-phase reaction and gas-solid thermal nonequilibrium in reverse combustion; Int. J. Heat mass Transfer 40 (1997) 2607–2620.
24. Tsotsas, E. and E. Martin: Thermal conductivity of packed beds, A review; Chem. Eng. Process 22 (1987) 19–37.
25. Kaviany, M.: Principles of Heat Transfer in Porous Media; second edition, Springer Publishers, New York, 1995.
26. Gunn, D.J.: Axial and radial dispersion in fixed beds; Chem. Eng. Sci. 42 (1987) 363–373.
27. Vortmeyer, D.: Axial heat dispersion in packed beds; Chem. Eng. Sci. 30 (1975) 999–1001.
28. Koch, D.L., and J.F. Brady: Dispersion in fixed beds; J. Fluid Mech. 154 (1985) 399–427.
29. Edwards, M.F., and J.E. Richardson: Gas dispersion in packed beds; Chem. Eng. Sci. 23 (1968) 109–123.
30. Wakao, N., and T. Funazkri: Effect of fluid dispersion coefficients on particle-to-fluid mass transfer coefficients in packed beds; Chem. Eng. Sci. 33 (1978) 1375–1384.
31. Martin, H.: Low Peclet number particle-to-fluid heat and mass transfer in packed beds; Chem. Eng. Sci. 33 (1978) 913–919.
32. Grober, H. and S. Erk: Fundamentals of Heat Transfer; Mc Graw Hill, New York, 1961.
33. Singh, B.P., and M. Kaviani: Effect of solid conductivity on radiative heat transfer in packed beds; Int. J. Heat Mass Transfer 16 (1994) 2579–2583.
34. Fatehi, M. and M. Kaviany: Role of gas-phase reaction and gas-solid thermal nonequilibrium in reverse combustion; Int. J. Heat mass Transfer 40 (1997) 2607–2620.
35. Fuller, E.N., P.D. Schettler, and J.C. Giddings: A new method for prediction of binary gas-phase diffusion coefficient; Industrial and Engineering Chemistry 58 (1966) 19–27.
36. R.H. Perry and D.W. Green: Perry's Chemical Engineers' Hand Book; seventh edition, McGraw Hill, N.Y., 1997.
37. Peters, B. and C. Bruch: Drying and pyrolysis of wood particles: experiments and simulation; J. Anal. Appl. Pyrolysis 70 (2003) 233–250.
38. Doormal, V. and G.D. Raithby: Enhancements of the SIMPLE method for predicting incompressible fluid flow; Numer. Heat Transfer 7 (1984) 147–163.
39. Ferziger, J.H. and M. Peric: Computational Methods for Fluid Dynamics, second edition, Springer-Verlag, Berlin, 1999, pp. 74-75.
40. FLUENT 6.0; UDF Manual, Fluent Inc, New Hampshire, 2001.
41. Baker, R.R.: Temperature variation within a cigarette combustion coal during the smoldering cycle; High Temp. Sci. 7 (1975) 236–247.
42. Muramatsu, M., S. Umemura, and T. Okada: Consumption of oxygen and heat evolved during natural smolder of a cigarette; J. Chem., Soc. Japan, Chem. Ind. Chem. (1978) 1441–1448.
43. Baker, R.R. and D.F. Robinson: Semi-theoretical model for prediction of smoke deliveries; *in*: Papers Presented at the Joint Meeting of the Smoke and Technology Groups, Harare, Zimbabwe, October 1994, CORESTA Congress, Paris, 1994, pp. 63.
44. Norman, A.: Cigarette design and materials; *in*: Tobacco Production, Chemistry and Technology, edited by D.L. Davis and M.T. Nielsen, Blackwell Science Ltd., MA, 2002, Chapter 11B, pp. 353–387 .
45. Saidi, M.S., F. Rasouli, and M.R. Hajaligol: Heat transfer coefficient for a packed bed of shredded materials at low peclet numbers; Heat Transfer Engineering 27 (2006) 41–49.

Corresponding author:

Mohammad R. Hajaligol
Philip Morris USA Research Center,
Richmond, Virginia,
USA
E-mail: Mohammad.R.Hajaligol@pmusa.com